Phase transition induced recrystallization and low surface potential barrier leading to 10.91%-efficient $CsPbBr_3$ perovskite solar cells

Guoqing Tong[a,b], Taotao Chen[b], Huan Li[b], Longbin Qiu[a], Zonghao Liu[a], Yangyang Dang[a], Wentao Song[a], Luis K. Ono[a], Yang Jiang[b,*], and Yabing Qi[a,*]

[a] *Energy Materials and Surface Sciences Unit (EMSSU), Okinawa Institute of Science and Technology Graduate University (OIST), 1919-1 Tancha, Onna-son, Kunigami-gun, Okinawa 904-0495, Japan*

[*]E-Mail: Yabing.Qi@OIST.jp

[b] *School of Materials Science and Engineering, Hefei University of Technology, Hefei 230009, P. R. China*

[*]E-Mail: apjiang@hfut.edu.cn

ABSTRACT:

High efficiency and long-term stability are vital for further development of perovskite solar cells (PSCs). PSCs based on cesium lead halide perovskites exhibit better stability but lower power conversion efficiency (PCE), compared with organic-inorganic hybrid perovskites. Lower PCE is likely associated with trap defects, overgrowth of partial crystals and irreversible phase transition in the films. Here we introduce a strategy to fabricate high-efficiency $CsPbBr_3$-based PSCs by controlling the ratio of CsBr and $PbBr_2$ to form the perovskite derivative phases ($CsPb_2Br_5$/Cs_4PbBr_6) via a vapor growth method. Following post-annealing, the perovskite derivative phases as nucleation sites transform to the pure $CsPbBr_3$ phase accompanied by crystal rearrangements and retard rapid recrystallization of perovskite grains. This growth procedure induced by phase transition not only makes the grain size of perovskite films more uniform, but also lowers the surface potential barrier existing between the crystals and grain boundaries. Owing to the improved film quality, a PCE of 10.91% was achieved for n-i-p structured PSCs with silver electrodes, and a PCE of 9.86% for hole-transport-layer-free devices with carbon electrodes. Moreover, the carbon electrode-based devices exhibited an excellent long-term stability and retained 80% of initial efficiency in ambient air for more than 2000 h without any encapsulation.

Keywords

Perovskite solar cell, derivative phases, $CsPbBr_3$, phase transition, recrystallization, vapor deposition

1. Introduction

The incredible development of organic-inorganic hybrid perovskite solar cells (PSCs) in the past decade has attracted tremendous attention from both academia and industry. From the initial power conversion efficiency (PCE) of 3.8% to the very recently certified record of 24.2%[1-5], processing technique including solution method[6-8], vapor deposition[9-12], hybrid deposition[13-15], hybrid chemical vapor deposition[16-22], methylamine gas based method[23-27], vapor & solution[28-30] and anti-solvent crystallization[24, 31] *etc*. have been employed to produce the highly crystalline and uniform perovskite films[32]. Unfortunately, volatility of the organic materials (MA^+/FA^+) and weak bonding energy between metal cations and halide anions render the organic-inorganic hybrid PSCs to decompose easily under condition such as humidity, heat, electric filed and light illumination, which impedes the commercial applications[7, 33, 34]. To alleviate the instability issue, the substitution of organic cations with inorganic ones such as cesium (Cs) and rubidium (Rb) to construct all inorganic perovskites has been demonstrated to effectively improve the stability of PSCs [29, 35].

$CsPbI_3$ as the representative material of the inorganic perovskite $CsPbX_3$ (X=Cl, Br and I) shows a suitable optical bandgap of 1.73 eV, and the champion PCE is up to 17.06%[36, 37]. However, the desired cubic perovskite phase (α-$CsPbI_3$) is only stable at high temperatures (＞300 ºC) and spontaneously transforms to the non-perovskite yellow phase (δ-$CsPbI_3$) under ambient environment[38, 39]. Although several strategies have been developed to improve the durability of $CsPbI_3$-based PSCs (e.g., HI induced growth, solvent-controlled, gradient Br doping *etc.*), the stability is still far away to meet the requirement for practical applications [33, 39, 40]. Currently, an all inorganic $CsPbBr_3$-PSC with a hole transport layer (HTL) free architecture is proposed by employing carbon paste as counter electrode with an initial PCE of 6.7%, which can

survive in the humid environment for 2640 h[41].The replacement of iodine (I) with a smaller atomic radius such as bromine (Br) can decrease the structure deviation, resulting in an effective enhancement of perovskite durability[42]. However, the low PCE of $CsPbBr_3$-based PSCs is still an important issue due to the large optical absorption loss from the wide bandgap and severe recombination caused by inferior film quality.

To overcome these drawbacks, several strategies have been proposed to improve the overall PCE and simultaneously prolong the thermal stability of inorganic PSCs. For example, gradient architecture to accelerate hole extraction [40, 42-44], interface modification (i.e., derivative phases, quantum dots, ions doping B-site) to prolong carrier lifetimes [45, 46]. Regarding to the recombination, a high number of defects at the interface and grain boundaries usually act as charge recombination centers in the devices because the decomposition of crystals at the grain boundaries is more easily than that in the inner of the film seven under a lower temperature and/or humid condition, which significantly impedes charge carrier transport, resulting in a poor performance [47]. On the other hand, different with hybrid perovskites treated in a lower post-annealing temperature, a higher temperature treatment over 300 ^{o}C are necessary for the inorganic counterparts, which results in a fast and straight forward growth of crystals, leading to a poor crystallintiy with uneven crystal size, large traps and stress concentration in the films. Thus, it is important to fabricate high quality $CsPbBr_3$ films with a reduced defect density, uniform grain sizes to achieve highly efficient of $CsPbBr_3$-based PSCs.

In this work, we propose a phase transition induced (PTI) method to produce high quality $CsPbBr_3$ thin films by utilizing the derivative phases as nucleation sites to slow down the formation of $CsPbBr_3$ grains and release the stress concentration in order to achieve a high quality and compact perovskite film. In this method, core-shell structured films containing derivative phases, i.e., $CsPbBr_3$@$CsPb_2Br_5$ and $CsPbBr_3$@Cs_4PbBr_6 are first deposited on the substrates by the sequential vapor deposition method. After that, thermal annealing induced phase transition enables the formation of cubic $CsPbBr_3$ recrystallization films (denoted as PTI-$CsPbBr_3$) from

$CsPb_2Br_5$ and Cs_4PbBr_6 to novel $CsPbBr_3$ at the grain boundaries. Based on this growth procedure, the PTI-$CsPbBr_3$ films showed larger grain size, improved uniformity with high crystallization and a reduced trap density, as well as lower surface potential barrier between the crystals and grain boundaries. As a result, a champion PCE of 10.91% was achieved for n-i-p structured $CsPbBr_3$-based PSCs, and a PCE of 9.86% was also realized for HTL-free carbon electrode based PSCs. Furthermore, the carbon electrode based PSC exhibits a markedly stability improvement in both humidity and thermal attacks and retains 80% of initial performance after 2000 h.

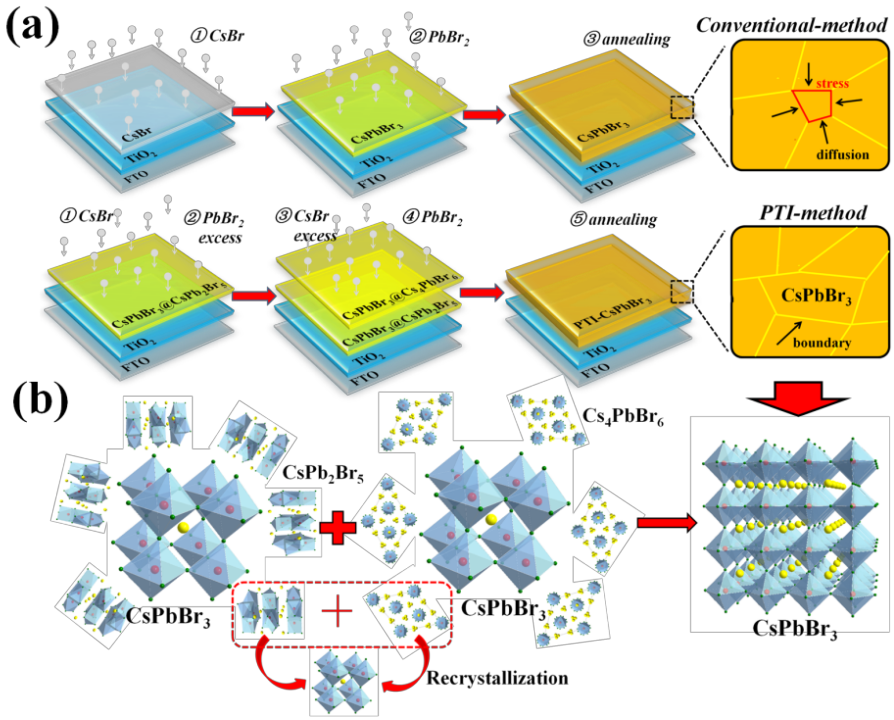

Fig. 1. (a) The conventional and phase transition induced (PTI) methods for the $CsPbBr_3$ thin film; (b) The formation from the derivative phase ($CsPb_2Br_5$/Cs_4PbBr_6) to the $CsPbBr_3$ inorganic perovskite phase.

2. Results and discussion

2.1 Characterization of PTI-$CsPbBr_3$ thin films and phase transition

Fig. 1a illustrates the formation of the $CsPbBr_3$ films by the conventional and PTI methods. Different from the conventional deposition procedure, we first prepare the $CsPbBr_3$@$CsPb_2Br_5$ core-shell structured layer by sequentially depositing the CsBr and

excess $PbBr_2$ in the PTI-method. Atop the $CsPbBr_3$@$CsPb_2Br_5$ layer, we deposit excess CsBr and $PbBr_2$ by sequential vapor deposition to form the $CsPbBr_3$@Cs_4PbBr_6 thin film. As seen in **Fig. S1**, the co-existence phases can be found in the pristine films and the corresponding atomic ratios of each element extracted from XPS measurements listed in **Table S1**, which agrees with our previous results[42, 47, 48]. **Fig. 1**b shows the corresponding phase transformation schematic drawing, in which $CsPbBr_3$ shows a three-dimensional (3D) cubic phase. $CsPb_2Br_5$ presents a two-dimensional (2D) tetragonal structure, and the Cs ions are sandwiched between two layers of Pb-Br coordination polyhedrons [47]. In turn, Cs_4PbBr_6 has a zero-dimensional (0D) crystal structure based on the $[PbBr_6]^{4-}$ octahedron, in which the octahedrons are separated from each other by CsBr bridges [48]. The presence of the derivative phases (i.e., $CsPb_2Br_5$ and Cs_4PbBr_6) around the $CsPbBr_3$ crystals facilitate the inorganic perovskite film formation during the post-annealing process, which is ascribed to inter-diffusion of the excess $PbBr_2$ in the $CsPb_2Br_5$ and excess CsBr in Cs_4PbBr_6 phase.

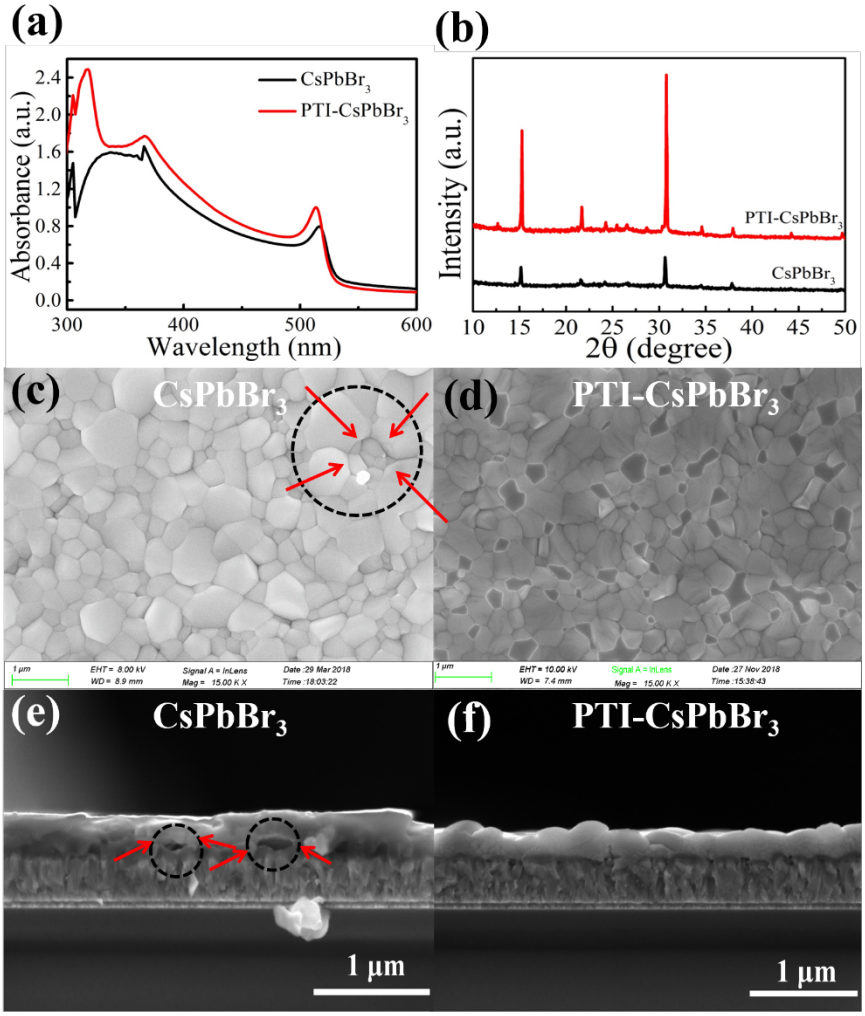

Fig. 2. (a) Absorption spectra and (b) XRD patterns of the $CsPbBr_3$ and PTI-$CsPbBr_3$ films; Scanning electron microscopy (SEM) images of (c) the $CsPbBr_3$ and (d) PTI-$CsPbBr_3$ films; Cross-section SEM images of (e) the $CsPbBr_3$ and (f) PTI-$CsPbBr_3$ films.

To get detailed understanding of the above proposed phase transformation process, we carefully check the photophysics, morphological and crystallographic properties of $CsPbBr_3$ and PTI-$CsPbBr_3$ films. **Fig. S4-S5** show the optical images of the $CsPbBr_3$ and PTI-$CsPbBr_3$ films annealed under different temperatures. It is observed that both cases turn into dark yellow with increasing the annealing temperature, and becomes light yellow at a higher temperature. As seen in **Fig. S6**, when the temperature is above 350 ºC, the absorption of the films decreased significantly due to the large pinholes (**Fig. S7-S8**). **Fig. 2**a shows the absorption spectra of the $CsPbBr_3$ and PTI-$CsPbBr_3$ films, in which the stronger light absorption at the short wavelength can be explained

by the high crystallinity and uniform grain size. The absorption edge of both films is located at ~ 550 nm, which is consistent with previous reports via the solution method [41, 49]. The corresponding optical bandgap values of the conventional $CsPbBr_3$ and PTI-$CsPbBr_3$ films are determined to be 2.35 and 2.37 eV, respectively, from a plot of $(\alpha h\nu)^2$ versus the photon energy ($h\nu$) using the Kubelka-Munk equations (**Fig. S9**) [50]. The negligible bandgap change indicates that the derivative phase converts to the $CsPbBr_3$ phase after annealing. Accompanied by the grain growth during the annealing procedure, we also find that the morphologies of the pre-preparation films are quite different at various annealing temperatures. In **Fig. S7-S10**, the uniform and compact films with gradually enlarged grain sizes are observed by the increase of annealing temperature (above 300 ^oC), compared to the pristine films at room temperature (RT). However, many pinholes can be found in the films after the treatment at an even higher temperature due to the decomposition of the inorganic perovskite, which significantly affects the light harvesting and forms the leakage path. Different from the conventional $CsPbBr_3$ film at the RT with a grain size of ~200 nm, the PTI-$CsPbBr_3$ film shows a smaller grain size, which is attributed to the top layer of $CsPbBr_3@Cs_4PbBr_6$ with lower crystallinity. Interestingly, as the annealing temperature increases, the grains of PTI-$CsPbBr_3$ grow quickly with high crystallinity in the film and much smaller crystallites can be detected clearly at the grain boundaries, which are formed by the phase transition. On the basis of the EDS spectra (in **Fig. S11**), it can be inferred that the ratio of Cs, Pb and Br is closed to 1:1:3, which suggests that the materials at grain boundaries correspond to the newly formed $CsPbBr_3$ crystallites as the result of phase transition. In parallel, it is worth noting that the grain size of the PTI-$CsPbBr_3$ film is significantly more uniform after annealing, as can be seen in **Fig. 2**d. On the contrary, overgrowth of partial crystals in the conventional $CsPbBr_3$ film (**Fig. 2**c) is observed due to fast reaction and uneven growth. The grain sizes are increased by the grain boundary diffusion during annealing. As large grains come into contact with each other and grow further, the grains extrude each other as illustrated in **Fig. 2**c (the red line indicates the direction of grain boundary diffusion), which impedes the grain boundaries diffusion and results in the stress concentration at the grain boundaries. In

the SEM cross-section images (**Fig. 2**e-f), we can see that the conventional $CsPbBr_3$ film has a full coverage but poor crystallinity. The extrusion of the grains against each other results in partial convex grains, leaving a large number of pinholes between the substrate and $CsPbBr_3$ film. In contrast, the PTI-controlled film exhibits a high crystallinity, uniform and full coverage film after post-annealing. To further understand the component and phase transition of inorganic perovskite, we analyze the X-ray diffraction (XRD) patterns of pre-films at different annealing temperatures with/without the PTI treatment. As presented in **Fig. 2**b and **Fig. S12-S15**, for the conventional $CsPbBr_3$ film, the typical peaks at 15.20°, 21.55°, 30.66°, 34.37° and 37.77° are detected and can be assigned to (100), (110), (200), (210) and (211). In turn, the $CsPbBr_3$ film grown by the PTI method is substantially different. At the room temperature (RT) condition, partial CsBr and $PbBr_2$ can't react completely, resulting in a derivative phase in the film. The peaks at 11.65°, 24.05°and 29.38° can be assigned to the $CsPb_2Br_5$ phase and other diffraction peaks located at 22.41° and 28.60° are assigned to Cs_4PbBr_6 (**Fig. S12**). As the annealing temperature increases, the peaks become shaper, which indicates that the high annealing temperature can accelerate the inter-diffusion and reaction of CsBr and $PbBr_2$ to form the pure $CsPbBr_3$ and also promote the crystal growth into larger grains. On the other hand, many crystallites exist in the perovskite grains because of the polycrystalline nature of the perovskite films. It is worth noting that the full-width at half-maximum (FWHM) of (100) and (200) reflections decreases after the PTI treatment. The corresponding crystallite sizes are determined by using Scherrer equation (see in **Table S2**), and the crystallinites size increase from 68.01 nm and 57.73 nm to 94.25 nm and 69.65 nm, respectively, which indicates that large crystallite sizes are obtained in the PTI-$CsPbBr_3$ grains. We also find that the PL spectra of the PTI-$CsPbBr_3$ films are enhanced gradually as the annealing temperature increases and drops remarkably after being treated at even higher temperatures (**Fig. S16**). It is reported that $CsPb_2Br_5$ and Cs_4PbBr_6 are the indirect bandgap materials with PL forbidden by their symmetry [51-53]. The corresponding lifetime of PTI-$CsPbBr_3$ films are increased from 1.03 ns to 4.45 ns after annealing at 350 °C for 30 min (in **Fig. S16**). This improvement indicates that the high

quality perovskite films provide high crystallinity and fewer traps at the grain boundaries after post-annealing.

How to understand the rearrangement of crystals induced by the phase transition? Firstly, Cs_4PbBr_6 can be viewed as the CsBr-rich component material and transformed into the cubic $CsPbBr_3$ phase with a side-product of CsBr at the grain boundary in the humid and heat treatment as follows:[53] $Cs_4PbBr_6 \rightarrow CsPbBr_3+3CsBr$. Additionally, CsBr has a higher melting point above 600 ^oC, thus it can't be evaporated during the annealing process. In contrast, the annealing temperature (from RT to 450 ^oC) accelerates the diffusion of CsBr into the inner film. Similarly, $CsPb_2Br_5$ is regarded as the CsBr-deficient material (or the $PbBr_2$-rich material) and can be converted into the $CsPbBr_3$ phase with the presence of $PbBr_2$ at the grain boundary under post-treatment with a heating temperature above 300 ^oC[54]. The equation can be described as follows:[47] $CsPb_2Br_5 \rightarrow CsPbBr_3+PbBr_2$. It is worth noting that $PbBr_2$ has a melting temperature close to 357^oC, which ensures the chemical component and promotes its reaction with excess CsBr to construct the new $CsPbBr_3$ phase, if the treatment at a moderate temperature of ~350 ^oC[55]. Upon further annealing treatment ($>$400^oC), the sublimation of $PbBr_2$ and also the decomposition of $CsPbBr_3$ occur, which significantly influence the coverage of the obtained thin film, such as leaving pinholes in the film. This process can be described by the following equation: $CsPbBr_3 \rightarrow CsBr+PbBr_2$. A moderate annealing temperature ensures the complete reaction between $CsPb_2Br_5$ and Cs_4PbBr_6 to form the novel $CsPbBr_3$ at the ground boundaries as well as benefits the crystal growth into lager grains. As seen in **Fig. 3**b, during the annealing process, the derivative phase can serve as extra heterogeneous nucleation sites, which effectively slow down the formation of $CsPbBr_3$ crystals. Because the highly crystalline $CsPbBr_3$ is formed by reaction process between $CsPb_2Br_5$ and Cs_4PbBr_6, instead of fast growth of $CsPbBr_3$ directly. This effectively retards the perovskite growth rate, which markedly enhances the $CsPbBr_3$ film quality with lower traps than in the case of the inadequate reaction/fast reaction. On the other hand, this phase transition from 2D-$CsPb_2Br_5$ and 0D-Cs_4PbBr_6 to 3D structure of

$CsPbBr_3$ provides enough space for the perovskite grains to release the stress concentration, which is beneficial for reducing the surface potential.

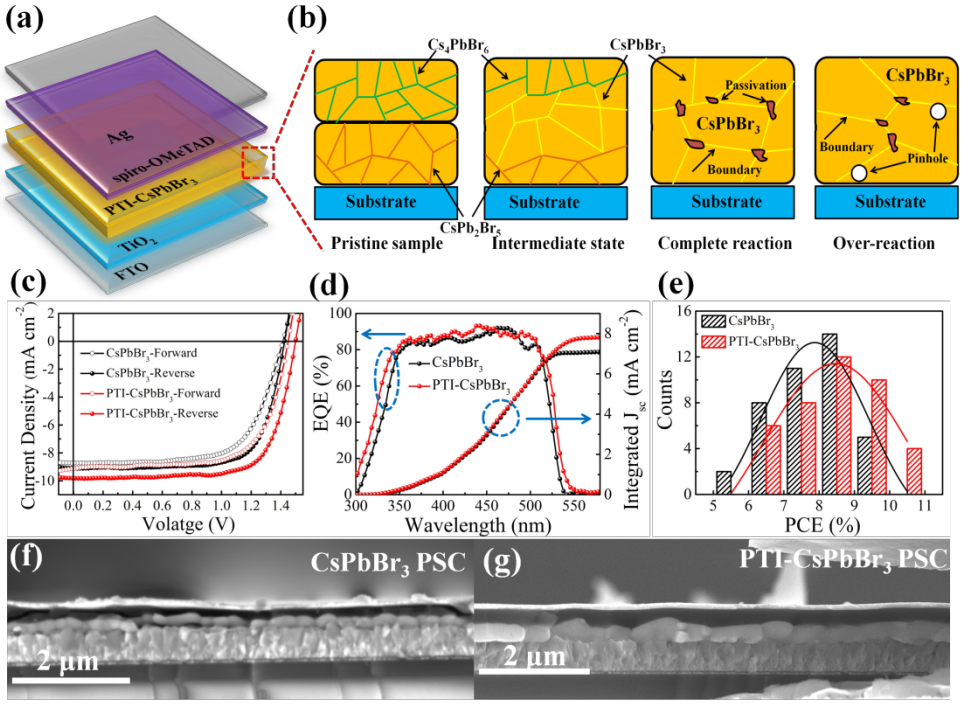

Fig. 3. (a) Device structure of a PTI-$CsPbBr_3$PSC; (b) Phase transition mechanism; (c) J-V curves of the $CsPbBr_3$ PSC and PTI-$CsPbBr_3$ PSC under forward and reverse scanning; (d) The corresponding EQE spectra and integrated J_{sc}; (e) Histograms of the PCEs of 40 devices for the $CsPbBr_3$ PSC and PTI-$CsPbBr_3$ PSC; Cross section SEM images of (f) the $CsPbBr_3$ PSC and (g) PTI-$CsPbBr_3$ PSC.

Table 1

Performance of the champion devices ($CsPbBr_3$ and PTI-$CsPbBr_3$) under forward and reverse scanning.

Scanning	V_{oc} (V)	J_{sc} (mA cm^{-2})	FF (%)	PCE (%)
$CsPbBr_3$-Forward	1.414	8.58	68.91	8.36
$CsPbBr_3$-Reverse	1.423	9.35	71.63	9.53
PTI-$CsPbBr_3$-Forward	1.452	9.08	69.70	9.19
PTI-$CsPbBr_3$-Reverse	1.498	9.78	74.47	10.91

2.2 Photovoltaic performance of PTI-$CsPbBr_3$ PSCs

Conventional inorganic PSCs are constructed with a planar architecture of FTO/c-TiO_2/inorganic perovskite/spiro-OMeTAD/Ag (**Fig. 3**a). **Fig. 3**f-g show the cross-sectional-view SEM image of the inorganic PSCs. It is observed that the conventional $CsPbBr_3$ or PTI-$CsPbBr_3$ film with an approximate thickness of 300 nm is homogenous and dense and sandwiched between the electron transport layer of TiO_2 and hole transport layer of spiro-OMeTAD. The photovoltaic performances of inorganic $CsPbBr_3$ PSCs formulated by the PTI and conventional method are given in **Fig. S17-S18** and **Tables S3-S4**. It is found that the performance of devices increases significantly with suitable annealing temperature and drops after high thermal attacks. Thus, we can obtain an optimal annealing temperature of 350 ^oC to ensure a high photovoltaic performance for PSCs. As depicted in **Fig. 3**b, the lower annealing temperature is unable to promote the inter-diffusion of $CsPb_2Br_5$ and Cs_4PbBr_6 to achieve phase transition to $CsPbBr_3$ for PTI-$CsPbBr_3$ case, which results in poor light harvesting and carrier transport, leading to a low efficiency. Similarly, a high density of pinholes in the films after the treatment at a higher temperature results in a poor morphology, which can be explained by the decomposition of perovskite films. Furthermore, pinholes create shunting paths leading to a poor performance. The current density-voltage (J-V) curves for champion devices of PTI-$CsPbBr_3$and conventional $CsPbBr_3$ are shown in **Fig. 3**c. The open-circuit voltage (V_{oc}), photocurrent density (J_{sc}) and fill factor (FF) of PTI-$CsPbBr_3$ PSC increase considerably by 75 mV, 0.53 mA cm^{-2} and 2.84%, respectively. The corresponding PCE of the best performing device increases from 9.53% (V_{oc}=1.423 V, J_{sc}=9.35 mA cm^{-2} and FF=71.63%) to a breakthrough performance 10.91% (V_{oc}=1.498 V, J_{sc}=9.78 mA cm^{-2} and FF=74.47%) under reverse scanning. To our best knowledge, this value is the highest performance for the $CsPbBr_3$-based PSCs. The corresponding external quantum efficiencies (EQE) are carried out and presented in **Fig. 3**d. The photoresponse edges of the devices are close to 550 nm, which agrees with the absorption spectra and shows a slight red-shift. As previously reported[56, 57], the reflection of light by the electrode and/or the FTO substrate, or some other interfaces in the perovskite devices are not considered when performing UV-vis measurements of bare perovskite films may lead to the slight red-

shift of the EQE spectrum as compared with the absorption spectrum, which were observed in both our work and several previous works[49, 58, 59]. The EQE values for both cases, in the visible region from 300 nm to 500 nm, exceed 80% with an integrated photocurrent density of 7.09 mA cm^{-2} (conventional $CsPbBr_3$), and 7.81 mA cm^{-2} (PTI-$CsPbBr_3$), respectively. It is close to the photocurrent density extracted from J-V curves. Additionally, the steady PCE of devices approaching 9.01% and 10.35% for $CsPbBr_3$ and PTI-$CsPbBr_3$ PSCs, respectively, are recorded under a bias voltage at the maximum power point for 200 s (**Fig. S19**), which agrees well with the value from J-V curves. It should be noted that only minor hysteresis effects are observed in the J-V measurements for the devices (**Fig. 3**c). In addition, this PTI-procedure exhibits good reproducibility, as seen in **Fig. 3**e, the efficiency of PTI-$CsPbBr_3$ PSCs ranging from 6.5% to 10.9% for 40 devices and presents a relatively higher PCE than that of conventional $CsPbBr_3$ PSCs.

Additionally, we construct a solar cell device based on the HTL-free architecture employing the carbon as counter electrode (**Fig. 4**a), where the absence of organic HTL and the usage of carbon electrodes can improve the stability of PSCs [60-62]. The cross-sectional-view SEM image of the HTL-free device (**Fig. 4**b) shows that the continuous and uniform perovskite film with full coverage can effectively block the recombination between the absorption layer and carbon electrode, reducing the leakage path in PSCs. The observed good contact between the carbon paste and perovskite layer enables a high current extraction. As a result, an impressive PCE of 9.86% under forward scanning is obtained (**Fig. 4**c). The corresponding steady-state PCE is up to 9.15% as shown in **Fig. S20**. **Fig. 4**d and **Table S5** provide a comprehensive comparison of the PCE and device storage lifetime between this work and previously reported studies on $CsPbBr_3$-based PSCs [41, 45, 49,58, 63-71].

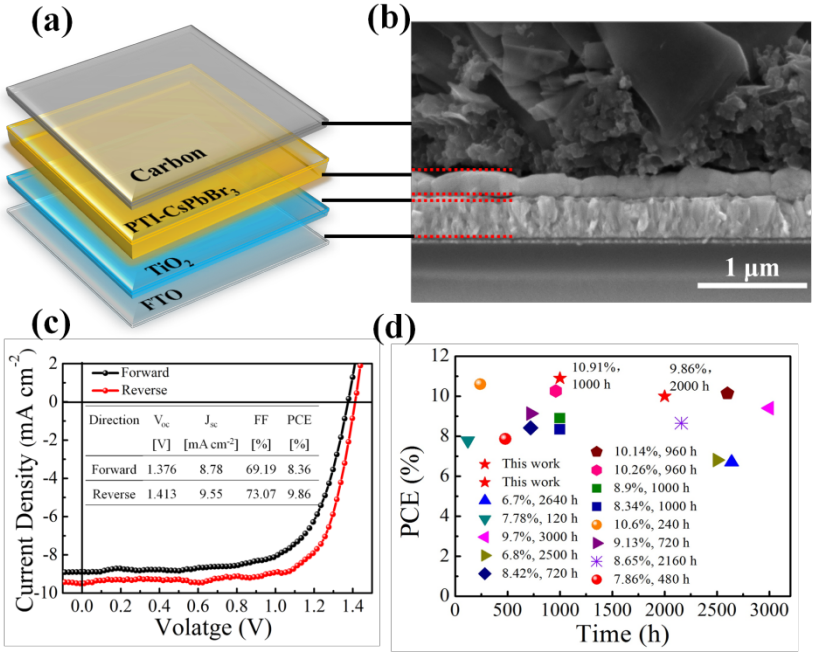

297

298 **Fig. 4.** Schematic drawing showing (a) the hole transport layer (HTL) free device structure of
299 thePTI-$CsPbBr_3$ and (b) the corresponding cross section SEM; (c) J-V curves of the PTI-$CsPbBr_3$
300 PSCs with HTL-free under forward and reverse scanning; (d) Comparison of the PCE and device
301 storage lifetime between this work and previously reported studies on $CsPbBr_3$-based PSCs. More
302 details can be found in Supplementary Table S5.

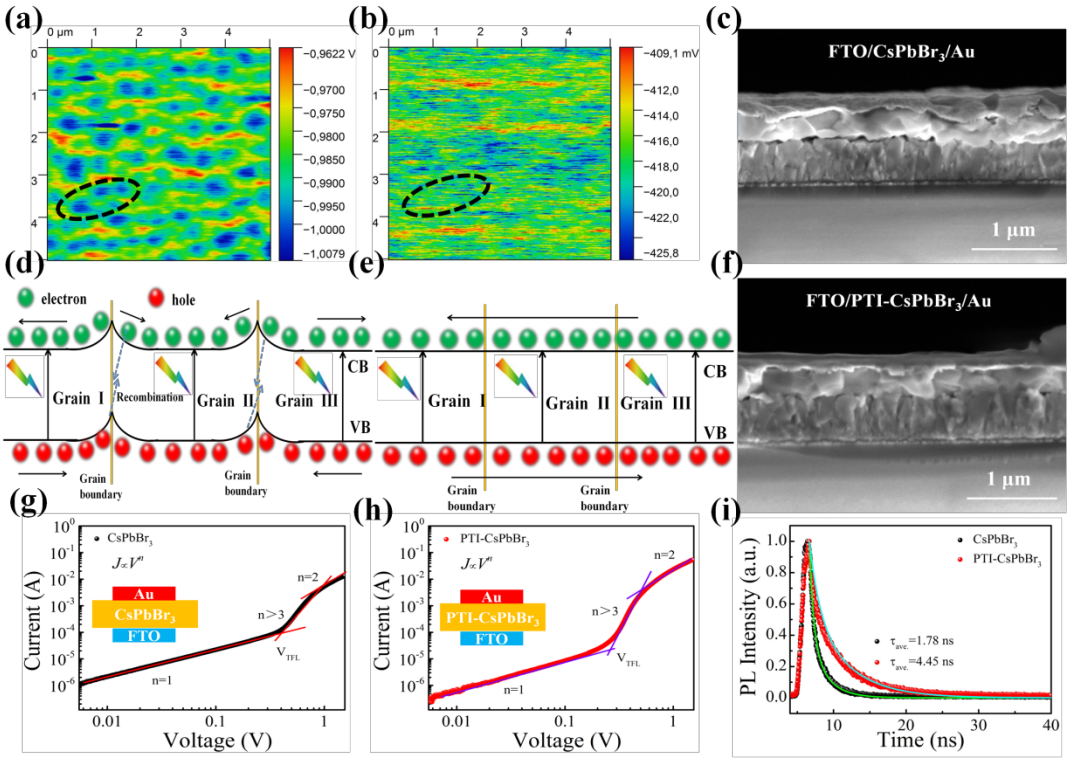

303

304 **Fig. 5.** Kelvin probe force microscopy (KPFM) images of (a) the $CsPbBr_3$ and (b) PTI-$CsPbBr_3$

films; (c) Cross section SEM images of the devices with FTO/$CsPbBr_3$/Au; Carrier transport mechanism of (d) the $CsPbBr_3$ and (e) PTI-$CsPbBr_3$ films; (f) Cross section SEM images of the devices with FTO/PTI-$CsPbBr_3$/Au; Current density-voltage (J-V) characteristics of devices with (g) the FTO/$CsPbBr_3$/Au and (h) FTO/PTI-$CsPbBr_3$/Au architecture; (i) Time resolved photoluminescence (TRPL) decay curves of the $CsPbBr_3$ and PTI-$CsPbBr_3$ films under 375 nm photon excitation.

2.3 Surface potential and carrier transport of PTI-$CsPbBr_3$ thin films

In general, the low PCE or poor stability of inorganic perovskite based PSCs are due to a large number of defects and unstable phases in the perovskite film during the formation. This is because the required high temperature annealing for the perovskite formation usually induce uneven growth of perovskite grains, which increases the stress concentration at the grain boundaries and also accelerates the overgrowth of partial perovskite crystals. Therefore, it may result in a large number of traps and metastable phase [30, 72, 73]. Thus we perform the surface investigation later to further understand the surface potential and carrier transport properties caused the rearrangement of crystals during the phase transition.

It is worth noting that the phase transition during the annealing processing providing a self-passivation at the grain boundaries, which shows a significant influence on the performance of devices. To further identify the self-passivation and understand the carrier transport behavior, we conduct a surface potential measurement by Kelvin probe force microscopy (KPFM). As shown in **Fig. S21**, the grain size of the PTI-$CsPbBr_3$ film is uniform, which provides an ultra-smooth surface with a root-mean-square roughness (RMS) of 13.75 nm. On the contrary, the grain size in the conventional $CsPbBr_3$ film is substantially larger and some grains are overgrown, which results in a substantially larger roughness of 20.55 nm. The surface potential mappings of the $CsPbBr_3$ films prepared by PTI and conventional method are presented in **Fig. 5**a-b and **Fig. S22**. The distribution of blue spots in the conventional $CsPbBr_3$ film is discontinuity and surrounded by the yellow patterns suggesting that the surface potential at the grain boundaries is higher than that in the crystals due to the overgrowth

of partial crystals (as depicted in **Fig. 1**a and **Fig. 2**c)[74]. However, the film produced by the PTI method giving a uniform distribution without any remarkable spots indicates that the lower surface potential barrier exists between the crystals and the grain boundaries. **Fig. S23** presents the contact potential difference (CPD) statistical distribution for conventional and PTI-$CsPbBr_3$ films. The absolute valueof average potentials for conventional $CsPbBr_3$ and PTI-$CsPbBr_3$ are 0.993 V and 0.418 V, respectively, which indicates that the PTI-$CsPbBr_3$ film shows a lower surface potential than the conventional $CsPbBr_3$ film. The potential barrier between the grain boundary and crystal implies a remarkable effect on the carrier transport. **Fig. 5**d-e show the schematic band diagrams for the conventional $CsPbBr_3$ and PTI-$CsPbBr_3$ film under illumination. The presence of three blue spots from the overgrown grains indicates that the three grains are connected with each other and the holes are accumulated at the grain boundary due to the existence of the potential barrier in the film. This accumulation will lower the valance and conduction band of the perovskite film at the grain boundaries, which impedes the electron transport and results in a large number of the recombination at the grain boundary [74,75]. In contrast, the appearance of the recrystallization phase at the grain boundary gives a uniform surface potential in the PTI-$CsPbBr_3$ film, which ensures the energy band consistency. It will benefit the electrons and holes transport to the counter electrode without any recombination at the grain boundaries. To verify this hypothesis , a time resolved photoluminescence (TRPL) is carried out and recorded in **Fig. 5**i. The curves are fitted by the equation: [65, 76]

$$\tau_{ave} = \frac{B_1\tau_1^2 + B_2\tau_2^2}{B_1\tau_1 + B_2\tau_2}$$

where B_1 and B_2 are the amplitudes, τ_1 and τ_2 represent the nonradioactive recombination and radiative recombination, respectively. The average lifetime of conventional $CsPbBr_3$ film is shorter than the PTI case, which confirms that the trap defects in the film are effectively suppressed by the recrystallization phases. To further evaluate the carrier transport behavior and defect density within the films, we construct a simple architecture by inserting the $CsPbBr_3$ thin film (with a thickness of 300 nm) between FTO and gold (FTO/inorganic perovskite/Au) as seen in **Fig. 5**c and f. The

evolutions of the space-charge limited current (SCLC) are tested under different bias voltage (**Fig. 5**g-h). The corresponding trap-filled limit voltages (V_{TFL}) can be extracted from the following equation:[24]

$$V_{TFL} = \frac{N_\tau e L^2}{2\varepsilon\varepsilon_0}$$

where N_τ is the trap density. ε is defined as dielectric constants of $CsPbBr_3$ perovskite (ε=16.46) and ε_0 is the vacuum permittivity with the value of 8.8×10^{-12} F • m^{-1}. The e and L are the electron charge, and the corresponding thickness of the perovskite film. Here the V_{TFL} of the conventional $CsPbBr_3$ and PTI-$CsPbBr_3$ devices are 0.40 V and 0.25 V, respectively. The corresponding defect densities are estimated to be 8.06×10^{15} cm^{-3} and 5.04×10^{15} cm^{-3} for the $CsPbBr_3$ film with/without PTI treatment, showing a significantly reducing defects traps due to the high crystallinity of perovskite films and boundary passivation after recrystallization.

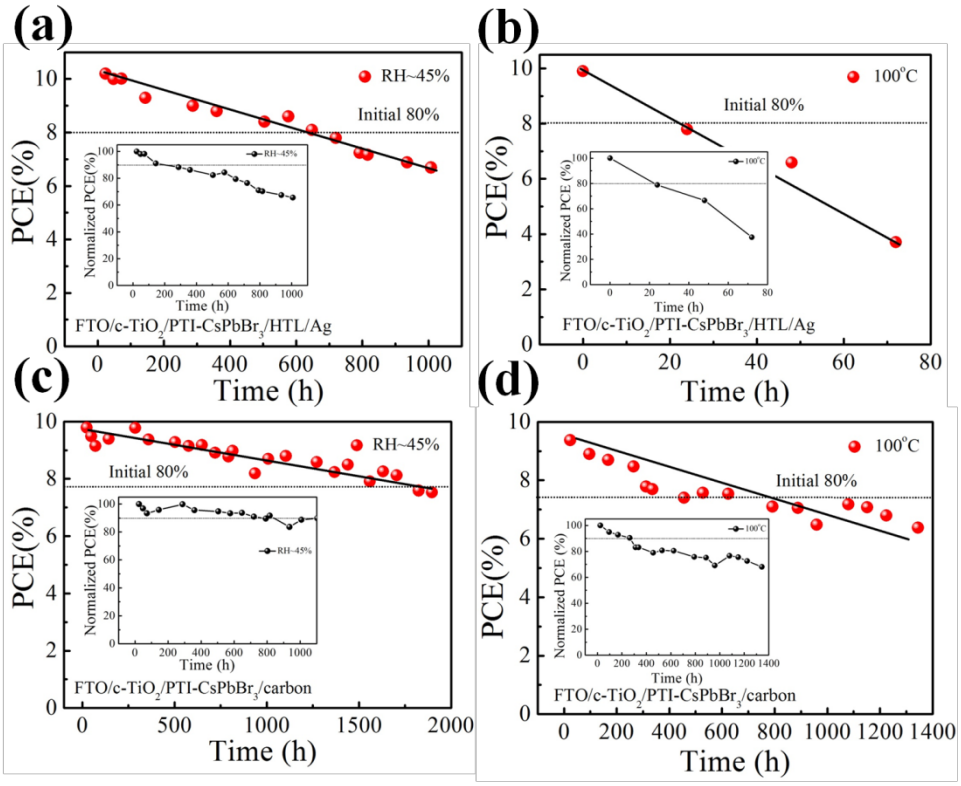

Fig. 6. Stability of PTI-$CsPbBr_3$ PSCs with HTL layer under (a) the humid environment (RH~45%) and (b) the heat condition (100°C); Stability of the PTI-$CsPbBr_3$ PSCs without HTL layer under (c) the humid environment (RH~45%) and (d) the heat condition (100°C).

2.4 Stability and degradation of PTI-$CsPbBr_3$ PSCs

Inorganic PSCs showing a good long-term stability, especially the $CsPbBr_3$-based devices, has been verified by previous reports and demonstrated with slight degradation under the high humid/heat condition [41, 49]. To check the stability of our devices, we track the stability in both persistent humid and heat condition without any encapsulation. As depicted in **Fig. 6**, the performance of the device with HTL layer drops significantly under the thermal attacks due to the invalidation of spiro-OMeTAD, instead of perovskite absorption layer. This is because the glass-transition temperature (T_g) of spiro-OMeTAD is only 122 ^oC [77]. After introducing the additive such as Li salt, the ideal working temperature of HTL layer would be less than 80 ^oC [78]. Compared with the high heating temperature, the low T_g would make much trap sites to be formed in the HTL layer [79]. Additionally, the metal electrode migration across the spiro-OMeTAD layer into perovskite layer will induce the degradation of perovskite film and form the leakage path [78]. These results can be verified by the XRD results in **Fig. S24a**, in which the sample still preserves the perovskite structure after being stored at 100 ^oC without any decomposition. In turn, the device with HTL stored in the open air can still keep 80% of initial PCE for more than 1000 h. Notably, the carbon-electrode-based device without HTL presents slight degradation in the humid environment (90% of initial PCE after 1000 h and 80% of initial PCE after 2000 h), which demonstrates that the high stability against the moisture. At the same time the device with carbon electrode also gives a superior performance at high temperature and keeps over 60% of initial PCE after stored in the thermal equipment at 100 ^oC for 1400 h. The corresponding XRD patterns in **Fig. S24b** and **Fig. S25b** show that the $CsPbBr_3$ films still keep high crystallinity after moisture and thermal attacks. The decrease of device performance may be ascribed to the damage the carbon electrode such as binder and conductive agent instead of the $CsPbBr_3$ films. Overall, these results demonstrate that $CsPbBr_3$ is the potential candidate in boosting the photovoltaic performance and stability of inorganic perovskite photovoltaic devices.

3. Conclusion

In summary, we report a phase transition induced strategy to prepare $CsPbBr_3$ inorganic perovskite films. By introducing the derivative phase of $CsPb_2Br_5$ and Cs_4PbBr_6 as nucleation sites, a highly crystalline $CsPbBr_3$ film is obtained via crystal rearrangement after annealing. The PTI-$CsPbBr_3$ film also provides uniform grain sizes and self-passivation at the grain boundaries, which lowers the potential barrier between the crystal and grain boundary and reduces the trap defects, facilitating carrier transport. Finally, we successfully achieve the highest PCE of 10.91% for the $CsPbBr_3$ based PSCs, which also show high stability (over 2000 h in humidity and 1400 h in heat condition) in moisture and thermal attacks environment.

Acknowledgements

This work was supported by funding from the Energy Materials and Surface Sciences Unit of the Okinawa Institute of Science and Technology Graduate University, the OIST R&D Cluster Research Program, the OIST Proof of Concept (POC) Program, and JSPS KAKENHI Grant Number JP18K05266. T. C., H. L and Prof. Y. Jiang acknowledge the National Natural Science Foundation of China No. U1632151, and the Open Research Fund of the State Key Laboratory of Pulsed Power Laser Technology of China (Hefei, SKL 2015 KF 04), and the Key Research and Development Project of Anhui Province of China (Grant No. 1704a0902023).

Appendix A. Supplementary material

Supplementary data associated with this article can be found in theonline version at http://dx.doi.org/10.1016/XXX.

References

[1] A. Kojima, K. Teshima, Y. Shirai, T. Miyasaka, J. Am. Chem. Soc.131 (2009), 6050-6051.

[2]https://www.nrel.gov/pv/assets/pdfs/best-research-cell-efficiencies-190416.pdf(2019).

[3] Q. Jiang, Y. Zhao, X. Zhang, X. Yang, Y. Chen, Z. Chu, Q. Ye, X. Li, Z. Yin,

J. You, Nat. Photonics.2019, DOI:10.1038/s41566-019-0398-2.

[4]S. Wu, R. Chen, S. Zhang, B. H. Babu, Y. Yue, H. Zhu, Z. Yang, C. Chen, W. Chen, Y. Huang, S. Fang, T. Liu, L. Han, W. Chen, Nat. Commun. 10(2019) 1161-1170.

[5] J. Xue, D. Yang, B. Cai, X. Xu, J. Wang, H. Ma, X. Yu, G. Yuan, Y. Zou, J. Song, H. Zeng, Adv. Funct. Mater.29 (2019) 1807922-1807929.

[6] D. Bi, W. Tress, M. I. Dar, P. Gao, J. Luo, C. Renevier, K. Schenk, A. Abate, F. Giordano, J. C. Baena, J. D. Decoppet, S. M. Zakeeruddin, M. K. Nazeeruddin, M. Grätzel, A. Hagfeldt, Sci. Adv. 2(2016) e1501170.

[7] Y. Zhao, H. Tan, H. Yuan, Z. Yang, J. Z. Fan, J. Kim, O. Voznyy, X. Gong, L. N. Quan, C. S. Tan, J. Hofkens, D. Yu, Q. Zhao, E. H. Sargent, Nat. Commun. 9(2018) 1607-1616.

[8] A. Swarnkar, A. R. Marshall, E. M. Sanehira, B. D. Chernomordik, D. T. Moore, J. A. Christians, T. Chakrabarti, J. M. Luther, Science 354(2016) 92-95.

[9] M. Liu, M. B.Johnston, H. J. Snaith, Nature 501(2013) 395-398.

[10] G. Tong, H. Li, G. Li, T. Zhang, C. Li, L. Yu, J. Xu, Y. Jiang, Y. Shi, K. Chen, Nano Energy 48(2018) 536-542.

[11] M. R. Leyden, L. K. Ono, S. R. Raga, Y. Kato, S. Wang, Y. B. Qi, J. Mater. Chem. A 2(2014) 18742-18745.

[12] J. Ávila, C. Momblona, P. P. Boix, M. Sessolo, H. J. Bolink, Joule 1(2017) 431-442.

[13] L. K.Ono,S. Wang, Y.Kato, S. R.Raga,Y. B. Qi, Energy Environ. Sci. 7(2014) 3989-3993.

[14] S. Wang, L. K. Ono, M. R. Leyden, Y. Kato, S. R. Raga, M. V. Lee, Y. B.Qi, J. Mater. Chem. A 3(2015) 14631-14641.

[15] S. Wang, X. Li, J. Wu, W. Wen, Y. B. Qi, Curr. Opin. Electrochem. 11(2015) 130-140.

[16] M. Leyden, L. K. Ono, S. Raga, Y. Kato, S. Wang, Y. B. Qi, J. Mater. Chem. A 2(2014) 18742-18745.

[17] M. R. Leyden, M. V. Lee, S. R. Raga, Y. B. Qi, J. Mater. Chem. A 2(2015)

16097-16103.

[18] M. R. Leyden, Y.Jiang, Y. B. Qi, J. Mater. Chem. A 4(2016) 13125-13132.

[19] L. K. Ono, M. R. Leyden, S. Wang, Y. B. Qi, J. Mater. Chem. A 4(2016) 6693-6713.

[20] M. R. Leyden, L. Meng, Y. Jiang, L. K. Ono, L. Qiu, E. J. Juárez-Pérez, C. Qin, C.Adachi, Y. B. Qi, J. Phys. Chem. Lett. 8(2017) 3193-3198.

[21] A. Ng, Z. Ren, Q. Shen, S. H. Cheung, H. C. Gokkaya, S. K. So, A. B. Djurisic, Y. Wan, X. Wu, C. Surya, ACS Appl. Mater. Interfaces 8(2016)32805-32814.

[22] G. Tong, Z. Song, C. Li, Y. Zhao, L. Yu, J. Xu, Y. Jiang, Y. Sheng, Y. Shi,K.Chen, RSC Adv.7(2017) 19457-19463.

[23] S. R. Raga, L. K.Ono, Y. B. Qi, J. Mater. Chem. A, 4(2016) 2494-2500.

[24] Z. Liu, L. Qiu, E. J. Juarez-Perez, Z. Hawash, T. Kim, Y. Jiang, Z. Wu, S. R. Raga, L. K.Ono, S. F. Liu, Y. B. Qi, Nat. Commun. 9(2018) 3880-3890.

[25] G. Tong, X. Lan, Z. Song, G. Li, H. Li, L. Yu, J. Xu, Y. Jiang, Y. Sheng, Y. Shi, K. Chen, Mater. Today Energy, 5 (2017) 173-180.

[26] S. Pang, Y. Zhou, Z. Wang, M. Yang, A. R. Krause, Z. Zhou,K. Zhu, N. P. Padture, G. Cui, J. Am. Chem. Soc. 138(2016) 750-753.

[27] S. R. Raga, Y. Jiang, L. K. Ono, Y. B. Qi, Energy Technology 5(2017) 1750-1761.

[28] Q. Chen, H. Zhou, Z. Hong, S. Luo, H-S. Duan, H-H. Wang, Y. Liu, G. Li, Y. Yang, J. Am. Chem. Soc. 136(2014) 622-625.

[29] Y. Jiang, M. R. Leyden, L. Qiu, S. Wang, L. K. Ono, Z. Wu, E. J. Juarez-Perez, Y. B. Qi, Adv. Funct. Mater. 28(2018) 1703835-1703847.

[30] G. Tong, X. Geng, Y. Yu, L. Yu, J. Xu, Y. Jiang, Y. Sheng, Y. Shi, K. Chen, RSC Adv. 7(2017) 18224-18230.

[31] M. Xiao, F. Huang, W. Huang, Y. Dkhissi, Y. Zhu, J. Etheridge, A. Gray-Weale, U. Bach, Y-B. Cheng, L. Spiccia, Angew. Chem. Int. Ed. 53(2014)9898-9903.

[32] K. L. Gardner, J. G. Tait, T. Merckx, W. Qiu, U. W. Paetzold, L. Kootstra, M. Jaysankar, R. Gehlhaar, D. Cheyns, P. Heremans, J. Poortmans, Adv. Energy Mater. 6(2016) 1600386.

[33] P. Wang, X. Zhang, Y. Zhou, Q. Jiang, Q. Ye, Z. Chu, X. Li, X. Yang,Z.Yin, J. You, Nat. Commun. 9(2018) 2225-2231.

[34] W. Tress, M. Yavari, K. Domanski, P. Yadav, B. Niesen, J. P. Correa Baena, A. Hagfeldt, M. Grätzel, Energy Environ. Sci. 11(2018) 151-165.

[35] J-W. Lee, D-H. Kim, H-S. Kim, S-W. Seo, S. M. Cho, N-G. Park, Adv. Energy Mater. 5(2015) 1501310-1501318.

[36] Y. Wang, T. Zhang, M. Kan, Y. Zhao, J. Am. Chem. Soc. 140(2018) 12345-12348.

[37] E. M. Sanehira, A. R. Marshall, J. A. Christians, S. P. Harvey, P. N. Ciesielski, L. M. Wheeler, P. Schulz, L. Y. Lin, M. C. Beard, J. M. Luther, Sci. Adv. 3(2017)e4204.

[38]B. Li, Y. Zhang, L. Fu, T. Yu, S. Zhou, L. Zhang, L. Yin,Nat. Commun. 9(2018) 1076-1083.

[39] T. Zhang, M. I. Dar, G. Li, F. Xu, N. Guo, M. Grätzel, Y. Zhao, Sci. Adv. 3(2017) e1700841.

[40] H. Bian, D. Bai, Z. Jin, K. Wang, L. Liang, H. Wang, J. Zhang, Q. Wang, S.Liu,Joule 2(2018) 1500-1510.

[41] J. Liang, C. Wang, Y. Wang, Z. Xu, Z. Lu, Y. Ma, H. Zhu, Y. Hu, C. Xiao, X. Yi, G. Zhu, H. Lv, L. Ma, T. Chen, Z. Tie, Z. Jin,J. Liu, J. Am. Chem. Soc. 138(2016) 15829-15832.

[42] G. Tong, T. Chen, H. Li, W. Song, Y. Chang, J. Liu, L. Yu, J. Xu, Y. B. Qi, Y. Jiang, Sol. RRL 3(2019) 1900030-1900098.

[43] Q. Ma, S. Huang, X. Wen, M. A. Green, A. W. Y. Ho-Baillie, Adv. Mater.6(2016) 1502202-1502206.

[44] C. Liu, W. Li, C. Zhang, Y. Ma, J. Fan, Y. Mai, J. Am. Chem. Soc. 140(2018) 3825-3828.

[45] W. S. Subhani, K. Wang, M. Du, X. Wang, S. F. Liu, Adv. Energy Mater. 9(2019)1803785-1803793.

[46] F. Wang, X. Jiang, H. Chen, Y. Shang, H. Liu, J. Wei, W. Zhou, H. He, W. Liu, Z. Ning, Joule 2(2018) 2732-2743.

[47] G. Tong, H. Li, D. Li, Z. Zhu, E. Xu, G. Li, L. Yu, J. Xu, Y. Jiang, Small 14(2018) 1702523-1702530.

[48] G. Tong, H. Li, Z. Zhu, Y. Zhang, L. Yu, J. Xu, Y. Jiang, J. Phys. Chem. Lett. 9(2018) 1592-1599.

[49] J. Duan, Y. Zhao, B. He, Q. Tang, Angew.Chem. Int. Ed. 57(2018) 3787-3791.

[50] M. Chen, M-G. Ju, A. D. Carl, Y. Zong, R. L. Grimm, J. Gu, X. C. Zeng, Y. Zhou, N. P. Padture,Joule 2(2018) 558-570.

[51] G. Li, H. Wang, Z. Zhu, Y. Chang, T. Zhang, Z. Song, Y. Jiang, Chem. Commun. 52(2016) 11296-11299.

[52] L. Wu, H. Hu, Y. Xu, S. Jiang, M. Chen, Q. Zhong, D. Yang, Q. Liu, Y. Zhao, B. Sun,Q. Zhao, Y. Yin, Nano Lett. 17(2017) 5799-5804.

[53] X. Chen, F. Zhang, Y. Ge, L. Shi, S. Huang, J. Tang, Z. Lv, L. Zhang, B. Zou, H. Zhong, Adv. Funct. Mater. 28(2018) 1706567.

[54] F. Palazon, S. Dogan, S. Marras, F. Locardi, I. Nelli, P. Rastogi, M. Ferretti, M. Prato, R. Krahne, L. Manna,J. Phys. Chem. C 121(2017) 11956-11961.

[55] I. Y. Zaitseva, I. S.Kovaleva, V. A. Fedorov,Russ. J. Inorg. Chem.51(2006) 619.

[56] Z. Chen, Q. Dong, Y. Liu, C. Bao, Y. Fang, Y. Lin, S. Tang, Q. Wang, X. Xiao, Y. Bai, Y. Deng, J. Huang, Nat. Commun. 8(2017) 1890.

[57] Z.Xiao, Q. Dong , C. Bi , Y. Shao , Y. Yuan, J. Huang, Adv. Mater. 26(2014) 6503.

[58] W. Chen, J. Zhang, G. Xu, R. Xue, Y. Li, Y. Zhou, J. Hou, Y. Li, Adv. Mater. 30(2018) 1800855-1800864.

[59] L. Zhou, X. Guo, Z. Lin, J. Ma, J. Su, Z. Hu, C. Zhang, S. F. Liu, J. Chang, Y. Hao, Nano Energy 60 (2019) 583-590.

[60] A. Mei, X. Li, L. Liu, Z. Ku, T. Liu, Y. Rong, M. Xu,M.Hu, J. Chen, Y. Yang, M. Grätzel, H. Han, Science 345(2014) 295-298.

[61] Z. Liu, M. Zhang, X. Xu, L. Bu, W. Zhang, W. Li, Z. Zhao, M. Wang, Y. Cheng, H. He, Dalton Trans. 44(2015)3967-3973.

[62] Z. Liu, A. Zhu, F. Cai, L. Tao, Y. Zhou, Z. Zhao, Q. Chen, Y. Cheng, H. Zhou, J. Mater. Chem. A 5(2017) 6597-6605.

[63] Y. Zhao, J. Duan, H. Yuan, Y. Wang, X. Yang, B. He, Q. Tang, Sol. RRL,3(2019)1800284-1800290.

[64] H. Li, G. Tong, T. Chen, H. Zhu, G. Li, Y. Chang, L. Wang, Y. Jiang, J. Mater. Chem. A 6(2018) 14255-14261.

[65] J. Duan, Y. Zhao, X. Yang, Y. Wang, B. He, Q. Tang, Adv. Energy Mater. 8(2018) 1802346-1802354.

[66] H. Yuan, Y. Zhao, J. Duan, Y. Wang, X. Yang, Q. Tang, J. Mater. Chem. A 6(2018) 24324-24329.

[67] J. Ding, J. Duan, C. Guo, Q. Tang, J. Mater. Chem. A 6(2018) 21999-22004.

[68] X. Liu, X. Tan, Z. Liu, H. Ye, B. Sun, T. Shi, Z. Tang, G. Liao, Nano Energy 56(2019) 184-195.

[69] H. Xu, J.Duan, Y. Zhao, Z. Jiao, B. He, Q. Tang, Journal of Power Sources 399(2018) 76-82.

[70] Q. Li, J. Bai, T. Zhang, C. Nie, J. Duan, Q. Tang, Chem. Commun. 54(2018) 9575-9578.

[71] J. Ding, Y. Zhao, J. Duan, B. He, Q. Tang, ChemSusChem 11(2018) 1432-1438.

[72] Y. Zong, Z. Zhou, M. Chen, N. P. Padture, Y. Zhou, Adv. Energy Mater. 27(2018) 1800997-1801005.

[73] T. Zhang, N. Guo, G. Li, X. Qian, Y. Zhao, Nano Energy 26(2016) 50-56.

[74] A. Dymshits, A. Henning, G. Segev, Y. Rosenwaks, L. Etgar,Sci. Rep. 5(2015) 8704-8709.

[75] L. K.Ono, Y. B. Qi, J. Phys. Chem. Lett. 7(2016) 4764-4794.

[76] H. Dong, Z. Wu, J. Xi, X. Xu, L. Zuo, T. Lei, X. Zhao, L. Zhang, X. Hou, A. K-Y. Jen, Adv. Funct. Mater. 28(2018) 1704836-1704844.

[77] B. Xu, J. Zhang, Y. Hua, P. Liu, L. Wang, C. Ruan, Y. Li, G. Boschloo, E. M. J. Johansson, L. Kloo, A. Hagfeldt, A. K-Y. Jen, L. Sun, Chem 2(2017)676-687.

[78] K. Domanski, J-P. Correa-Baena, N. Mine, M. K. Nazeeruddin, A. Abate, M. Saliba, W. Tress, A. Hagfeldt, M. Grätzel, ACS Nano 10(2016) 6306-6314.

590 [79] G-W. Kim, G. Kang, M. M. Byranvand, G-Y. Lee, T. Park, ACS Appl. Mater.
591 Interfaces 9(2017) 27720-27726.
592